Available online at www.sciencedirect.com
SCIENCE DIRECT
ELSEVIER
Icarus 172 (2004) 59–77
ICARUS
www.elsevier.com/locate/icarus

The jovian rings: new results derived from Cassini, Galileo, Voyager, and Earth-based observations

H.B. Throop [a,*], C.C. Porco [a,1], R.A. West [b], J.A. Burns [c], M.R. Showalter [d], P.D. Nicholson [c]

[a] *Southwest Research Institute, 1050 Walnut St, Ste 400, Boulder, CO 80302, USA*
[b] *Jet Propulsion Laboratory, 4800 Oak Grove Drive, Pasadena, CA 91109, USA*
[c] *Department of Astronomy, Cornell University, Ithaca, NY 14853, USA*
[d] *Space, Telecommunications, and Radioscience Laboratory, Stanford University, Stanford, CA 94305, USA*

Received 5 June 2003; revised 23 December 2003

Available online 8 March 2004

Abstract

Cassini's Imaging Science Subsystem (ISS) instrument took nearly 1200 images of the Jupiter ring system during the spacecraft's 6-month encounter with Jupiter (Porco et al., 2003, Science 299, 1541–1547). These observations constitute the most complete data set of the ring taken by a single instrument, both in phase angle (0.5°–120° at seven angles) and wavelength (0.45–0.93 μm through eight filters). The main ring was detected in all targeted exposures; the halo and gossamer rings were too faint to be detected above the planet's stray light. The optical depth and radial profile of the main ring are consistent with previous observations. No broad asymmetries within the ring were seen; we did identify possible hints of 1000 km-scale azimuthal clumps within the ring. Cassini observations taken within 0.02° of the ring plane place an upper limit on the ring's full thickness of 80 km at a phase angle of 64°. We have combined the Cassini ISS and VIMS (Visible and Infrared Mapping Spectrometer) observations with those from Voyager, HST (Hubble Space Telescope), Keck, Galileo, Palomar, and IRTF (Infrared Telescope Facility). We have fit the entire suite of data using a photometric model that includes microscopic silicate dust grains as well as larger, long-lived 'parent bodies' that engender this dust. Our best-fit model to all the data indicates an optical depth of small particles of $\tau_s = 4.7 \times 10^{-6}$ and large bodies $\tau_l = 1.3 \times 10^{-6}$. The dust's cross-sectional area peaks near 15 μm. The data are fit significantly better using non-spherical rather than spherical dust grains. The parent bodies themselves must be very red from 0.4–2.5 μm, and may have absorption features near 0.8 and 2.2 μm.

Keywords: Planetary rings; Jupiter; Photometry; Dust

1. Introduction

Jupiter's ring system was first detected optically by Voyager 1 in 1979. Since then it has been observed both from the Earth and by visiting spacecraft. Its low optical depth ($\tau \sim 10^{-6}$) makes it difficult to see next to the bright disk of Jupiter. The ring system itself is normally separated into three components: the outer 'gossamer' rings (1.81–3.2R_J, where $1R_J = 71{,}492$ km) fed by dust from Amalthea and Thebe (Burns et al., 1999), the flattened main ring (1.72–1.82R_J), and the torus-shaped 'halo' ring (1.40–1.72R_J). Dust almost certainly migrates between the ring systems, either inward due to plasma drag (Burns et al., 1984), or in either direction due to resonant charge variation (Horanyi and Cravens, 1996; Northrop et al., 1989).

The dust by which we observe the ring is generally thought to be short-lived, with lifetimes against loss for micron-sized grain on the order of months to millenia. This dust, therefore, is hypothesized to be supported in steady-state by the introduction of new dust into the ring system. The source of this dust is thought to be from macroscopic (mm- to km-sized) 'parent bodies' in the ring, which release dust during mutual collisions and when impacted by high-velocity meteoroids. The parent bodies, then, may constitute the majority of the ring system's mass, but a much smaller fraction of its surface area. Dynamical arguments suggest

* Corresponding author.
E-mail address: throop@boulder.swri.edu (H.B. Throop).
[1] Current address: Space Science Institute, 4750 Walnut St, Ste 205, Boulder, CO 80301, USA.

0019-1035/$ – see front matter
doi:10.1016/j.icarus.2003.12.020

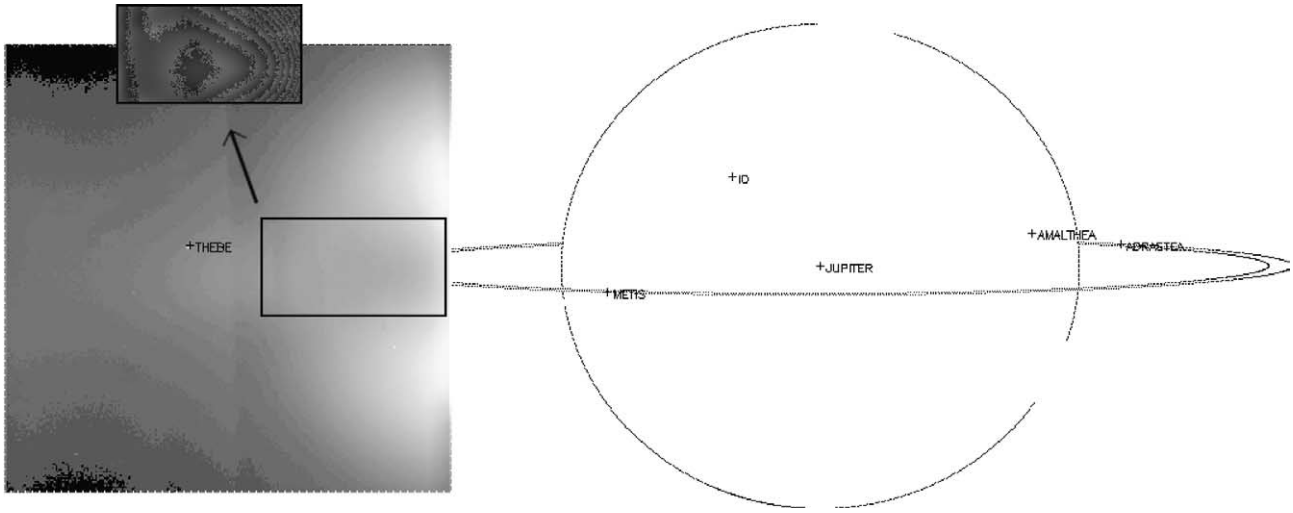

Fig. 1. Geometry for the inbound movie sequence, for phase angle $\alpha \sim 1°$ and ring opening angle $B \sim 3.4°$, December 11, 2000. This is a clear-filter image, 1 sec exposure, from $270 R_J$. Because the full disk of Jupiter is lit and the projected distance to the ring is $\sim 0.5 R_J$, the ring is visible above the stray light only after extensive processing. The 'wood grain' patterns in the inset image are artifacts of stray light removal over the lookup table used in compressing the image. Images in later sequences are less affected by stray light, because of Jupiter's increasing phase angle and the spacecraft's decreasing range (and thus increasing angular separation between the planet and its ring).

that they are the collisional remnants of a fragmented satellite (Canup and Esposito, 1997).

In this paper we present a complete report of the Cassini ISS observations of Jupiter's ring system, an initial analysis of which we reported on in Porco et al. (2003). We start with a summary of the observations and our methods of data reduction. We then present our new findings. In the final section, we combine the ISS results with nearly all previous observations of the main ring and present a new model for the size distribution of dust grains and large bodies within the ring.

2. New Cassini observations

The Cassini spacecraft was launched toward Saturn on October 15, 1997. After flybys of Venus and Earth, it flew past Jupiter, with a closest approach distance of $136 R_J$ on December 30, 2000 (Porco et al., 2003). The flyby was designed for trajectory modification and not scientific observations; therefore, the closest approach was many times farther than that of Voyager 1 ($4.89 R_J$) or Voyager 2 ($10.11 R_J$). Galileo's closest approach distance (while observing the rings) of $15.8 R_J$ provided 23 km pix^{-1} resolution and its limited number of images remain the best for studying the rings' morphology. Although the difficulties of observing at Cassini's distance are partially offset by its improved resolving power, the ISSs best spatial resolution in the ring of 58 km pix^{-1} is significantly coarser than Voyager's (5 km pix^{-1}). However, the Galileo Solid State Imager (SSI) investigation focused on morphology and returned no targeted color images; approximately half of the images are at forward-scatter (Sun-target-observer phase angle $\alpha \sim 180°$), limiting the studies that can be done on the ring's grain properties. The Galileo SSI observations were complemented by a spectral cube from the spacecraft's Near-Infrared Mapping Spectrometer (NIMS) in forward scatter (McMuldroch et al., 2000; Brooks et al., 2003), which allowed substantial constraints on the size distribution of its dust grains.

Earth-based studies of the ring are limited to a range in phase angle $\alpha = 0°$–$12°$, and are naturally much more difficult because Jupiter's disk—one million times brighter in reflected flux—lies only a fraction of an arc-minute away from the faint ring. Nevertheless, useful observations have been made in the near-IR using most of the major Earth-based observatories, as we describe in Section 4.

Targeted ISS observations of the jovian ring took place between December 11, 2000 and January 16, 2001. During these 5 weeks, Cassini's trajectory took it from 3.5° above the equator, to 3.2° below. On December 31, 2000 the spacecraft passed through Jupiter's ring plane; the spacecraft's closest approach to Jupiter occurred earlier the same day. Although the maximum ring opening angle was only $B = 3.5°$, this was in fact more open than observed by either Voyager ($B < 2.1°$) or Galileo ($B < 0.6°$), or by ground-based observations at ring plane crossing ($B < 0.2°$). In general, larger ring opening angles allow for higher-resolution mapping of the ring's morphology; however, smaller angles can allow for higher quality photometry because the ring's light is spread over fewer pixels. The inbound geometry is shown in Fig. 1, and typical images during the encounter are shown in Fig. 2. The supporting online material of Porco et al. (2003) contains additional details on the data collection and geometry of Cassini's flight by Jupiter.

The Cassini ISS instrument recorded a total of 1183 images of the main ring, providing broad coverage both in phase angle ($\alpha = 0.5°$–$120°$) and wavelength ($\lambda = 0.45$–0.93 μm). Because of the spacecraft's then-uncharacterized pointing stability, the ISS science team decided to focus predominantly on short exposures, generally shorter than 5 sec.

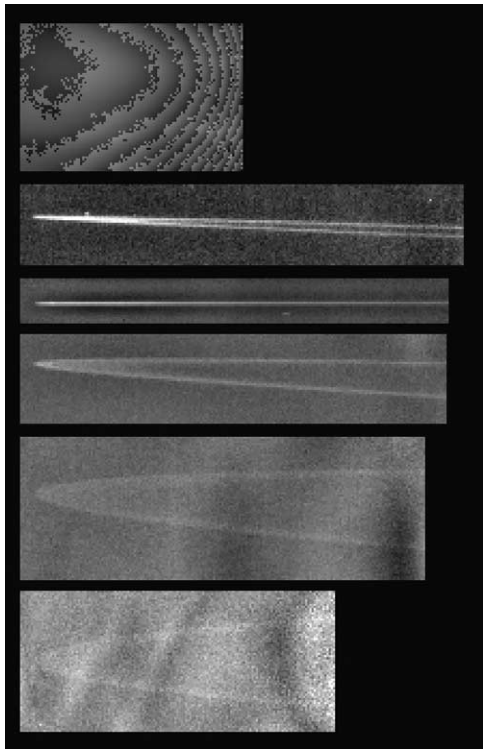

Fig. 2. The jovian ring as seen by Cassini from December, 2000—January, 2001. The phase angles are approximately 1°, 60°, 64°, 75°, 94°, and 120°, while the ranges are approximately $270\,R_J$, $137\,R_J$, $137\,R_J$, $141\,R_J$, $162\,R_J$, and $247\,R_J$. All images are taken through clear filters, with exposure lengths of several seconds. Stray light increases as Cassini leaves the system and the ring once again appears closer to Jupiter. The spatial resolution across these images varies from 120 km pix^{-1} at the ends, to 59 km pix^{-1} near the $136\,R_J$ closest approach. Images have been rescaled in brightness.

(By comparison, Voyager 1's discovery image of the ring was 11 min, and most of the remaining Voyager images were 96 sec. The Galileo images were generally shorter than 1 sec; however, these images were mostly taken very near $\alpha = 180°$, where the ring is nearly 100 times brighter and the planet is almost completely in shadow.) In retrospect, Cassini's pointing stability turned out to be excellent, and longer exposures would have increased the data quality. Images during most of the Cassini encounter rarely had more than a pixel of smear.

There were five major components to Cassini's observations, split amongst 14 spacecraft 'sequences' as listed in Table 1. First, the 'inbound movie' sequence (denoted RMOV000_PRIME_RING_B) was a 40-hour, 599-exposure sequence through the clear and near-IR filters, taken over $\alpha = 0.5°$–$2.5°$. This sequence was designed to look for temporal and spatial variations in the main ring ('spokes' and clumps), and to explore the ring's opposition effect. The ISS then began a suite of phase, spectral, and polarimetric observations of the ring, as the spacecraft traveled past the planet. At each of five phase angles (sequence RPHASE11R_CIRS_B at $\alpha = 11°$; RPHASE60L_VIMS_RIGHT_B and RPHASE60L_VIMS_LEFT_B at 60°; RPHASE75L_VIMS_RIGHT_B and RPHASE_75L_VIMS_LEFT_B at 75°; RPHASE_94L_VIMS_B at 94°; and RPHASE120L_VIMS_1X1 at 120°), observations were made across the entire wavelength range.[2] Third, the ring was imaged immediately after passing through the planet's equatorial plane, at an elevation $B = 0.02°$ and $\alpha = 64°$ (sequences RPLNXNG_PRIME_RIGHT_B and RPLNXNG_PRIME_LEFT_B). Fourth, the ISS made several deep exposures (up to 32 sec) of the area surrounding the gossamer rings at $\alpha = 120°$ (RPHASE120L_VIMS_1X3) in an attempt to probe for unknown rings in this region. Finally, the 36-hour 'outbound movie' sequence (RMOVOUT000_PRIME_RING) roughly repeated the observations of the inbound movie, at a higher phase angle ($\alpha = 120°$).

All of the ring images were taken using ISSs Narrow Angle Camera (NAC). The NAC is a 20-cm diameter reflector with a 1024 × 1024-pixel CCD array at its focal plane (Porco et al., in preparation). The camera's spatial scale is 6.0 μrad pix^{-1}, providing a 0.35° × 0.35° field-of-view. Multiple summation and compression modes are available on the instrument. For highest spatial resolution the FULL summation setting is used. To save bandwidth, however, many images used the 2 × 2 SUM2 or 4 × 4 SUM4 modes, where the data numbers (DN) in adjacent pixels are numerically summed before being read out by the instrument's analog-to-digital converter (ADC). (When we refer to the DN values of images taken in SUM2 or SUM4, we have scaled the returned DN value down by 4 or 16, respectively.) Images are also tagged by their conversion type: 12BI indicates that the full 12-bit resolution of the ADC is retained and sent to Earth, while LS8B indicates that only the least-significant 8 bits are kept. The TABLE mode indicates that the 12-bit resolution has been converted to 8 bits by use of a fixed, non-linear lookup table. The ISS Wide Angle Camera (WAC) was used for context observations of Jupiter's disk during the ring sequences, but because of its lower spatial resolution and poorer stray light rejection, it was not used for rings science observations.

2.1. Main ring

The ISSs inbound observations were significantly contaminated by stray light from Jupiter's bright disk. Typical ring signals are 1–2 DN on top of a stray light signal of 50–100 DN.

The stray light signal, while complex, can usually be removed such that accurate photometry can be performed on the ring images. The photometric pipeline we use is as follows: First, we radiometrically calibrate the images by converting the DN values into I/F, accounting for dark current, filter transmission, optics transmission, and CCD efficiency,

[2] Observations were originally scheduled for $\alpha = 24°$ and $\alpha = 45°$, but these were canceled due to temporary problems in the spacecraft's attitude control system. These problems also caused most of the $\alpha = 11°$ images to be smeared and poorly pointed.

Table 1
Jupiter ring observations by Cassini ISS NAC

Sequence	# Images	Time [UTC] (start, end)	Latitude [deg]	Range [R_J]	Phase [deg]	Resolution [km pix^{-1}] (NAC)	Filters	Ansa (as seen from Sun)	Comments
RMOV000_PRIME_RING_B	599	11-Dec-2000 13:47:20	3.47	284	2.5	122	CL, IR1, GRN, BL1	Left	Inbound movie
		13-Dec-2000 05:20:22	3.41	266	0.5	114			
RPHASE11R_CIRS_B	17	19-Dec-2000 02:06:09	2.63	203	10.9	87	CL, GRN, RED, BL1, UV2,	Right	Smeared due to thruster
		19-Dec-2000 02:16:43					IR1, IR2, IR3, P0, P60, P120		control
RPHASE24R_CIRS_B	0								Lost due to thruster
RPHASE45L_CIRS_B	0								control
RPHASE60L_VIMS_RIGHT_B	4	30-Dec-2000 10:32:10	0.21	137	59.7	59	CL, BL1	Right	
		30-Dec-2000 10:34:45							
RPHASE60L_VIMS_LEFT_B	19	30-Dec-2000 10:40:34	0.21	137	61.1	59	CL, GRN, RED, BL1, UV2,	Left	
		30-Dec-2000 10:52:54					IR1, IR2, IR3, P0, P60, P120		
RPLNXNG_PRIME_RIGHT_B	6	31-Dec-2001 01:08:10	−0.02	137	63.2	59	CL, BL1	Left [sic]	Ring plane crossing
		31-Dec-2000 01:13:06							
RPLNXNG_PRIME_LEFT_B	6	31-Dec-2000 01:36:10	−0.03	137	64.6	59	CL, BL1	Right [sic]	Ring plane crossing
		31-Dec-2000 01:41:04							
RPHASE75L_VIMS_RIGHT_B	6	2-Jan-2001 00:47:13	−0.66	142	75.3	61	CL, BL1	Right	
		2-Jan-2001 00:51:36							
RPHASE75L_VIMS_LEFT B	20	2-Jan-2001 00:55:33	−0.75	141	75.8	61	CL, GRN, RED, BL1, UV2,	Left	
		2-Jan-2001 01:09:17					IR1, IR2, IR3, P0, P60, P120		
RPHASE94L_VIMS_B	17	6-Jan-2001 00:02:04	−1.93	163	94.6	70	CL, GRN, RED, BL1, UV2,	Left	
		6-Jan-2001 00:12:54					IR1, IR2, IR3, P0, P60, P120		
RPHASE120L_VIMS_1X1	19	14-Jan-2001 23:02:19	−2.72	247	118	106	CL, GRN, RED, BL1, UV2,	Right (left from s/c)	
		14-Jan-2001 23:15:27					IR2, IR3, P0, P60, P120		
RPHASE120L_VIMS_1X3	15	14-Jan-2001 23:24:05	−2.72	247	118	106	CL, GRN, BL1, IR1	Right (left from s/c)	Gossamer ring search
		14-Jan-2001 23:51:06							
RMOVOUT000_PRIME_RING	455	15-Jan-2001 09:43:35	−3.13	252	119	108	CL	Right (left from s/c)	Outbound movie
		16-Jan-2001 21:15:32	−3.22	257	122	115			

The filter names are given in the standard Cassini convention; all observations were taken through a filter pair comprised of the named filter plus a clear filter.

based on ground-based and in-flight calibration standards. (I/F is the standard reflectance measurement for planetary bodies and rings; I indicates the intensity received at a detector looking at a body, while πF indicates the flux (usually solar) hitting that body. $I/F = 1$ for a white lambertian surface at normal incidence. For simplicity, we treat 'I/F' as a unit; for instance, $I/F(\lambda)$, rather than $I(\lambda)/F(\lambda)$.) We removed various instrumental artifacts including a 2-Hz signal introduced at readout and visible as a banding pattern in the faintest images. Geometric distortion in the NAC is negligible (< 1 pixel at image corners) and no correction is applied.

Second, we navigate the images using the locations of field stars in the frame and the spacecraft's known trajectory to determine the absolute coordinates of objects within the image. Third, we mask out the positions of any satellites and stars in the field, using their known locations. Fourth, we take a small rectangular subset of the frame containing the ring, and fit a two-dimensional spatial polynomial to subtract the background light from these pixels. (Experimentally, we found a fifth-order polynomial was preferable to either lower or higher orders. Because of the ring's faint signal relative to the background, it was not necessary to mask out the ring before performing the fit.) Finally, in all images except those near the ring-plane crossing, we create a radial profile of the ring, and subtract a linear offset such that the I/F at the ring's inner and outer edges is ~ 0. In images near the ring-plane crossing we instead subtract a constant offset such that the pixels surrounding the ring have $I/F \sim 0$, but do not take radial profiles. In both cases, the offset we subtract corrects for stray light not removed by the earlier polynomial subtraction.

By the end of this reduction process, we have created calibrated images, with the ring clearly visible, and with negligible contribution from background light sources. Our background subtraction process is not significantly influenced by the gossamer or halo rings; these rings are both vertically extended, and thus their values of I/F near the ring-plane crossing are 10–100 times lower than that of the main ring.

To quantify the ring's brightness, we use the 'normal I/F' (that is, the I/F that would be measured if the observation were taken from directly above the ring, but with the phase angle α preserved):

$$\frac{I}{F} \equiv \frac{\tau \varpi_0 P(\alpha)}{4\mu}, \tag{1}$$

where τ is the ring's normal optical thickness, ϖ_0 is the single-scattering albedo of a ring particle, $P(\alpha)$ is the ring's phase function, and $\mu = |\cos(e)|$. The emission angle is e, where $e = 0°$ for an observation directly above the ring plane. The elevation angle above the ring plane is $B \equiv 90° - e$. Following the convention of Showalter, we plot not I/F but $\tau \varpi_0 P$, and unless stated otherwise we will refer to the radially-averaged (not radially-integrated) brightness of the ring, taken over its 6500-km width.

Measuring the I/F from individual frames turned out to be often challenging, because of the low SNR and the complexities of the stray light removal. The errors associated with these issues are difficult to quantify, but on the lowest-quality individual frames (e.g., those from the inbound movie) the errors are certainly factors-of-several or more. The largest source of error in these images is stray light: the pattern changes from frame to frame, and even after the removal process stray light can contaminate the ring signal significantly in the faintest images. The best individual frames (e.g., $\alpha = 75°$ photometry, near closest-approach) can be processed to error levels of 10% or better; in this case, the error level is set predominantly by our ability to determine the zero-point of the background sky, and by uncertainty determining the ring's exact boundaries by stellar navigation. In most cases, multiple exposures taken at similar geometries and wavelengths allow us to combine I/F measurements and further reduce the uncertainty. Because of the frame-to-frame variation in stray light, I/F's were combined after initial image reduction, rather than summing the raw frames. The error bars are calculated from the standard deviation of the individual measurements. For spectral measurements, we have increased the error bars by 20% to account for our current uncertainties in the instrument's absolute spectral calibration (Porco et al., in preparation); the improved calibration expected during Cassini's upcoming years will reduce the I/F uncertainty.

2.1.1. Phase curve and spectrum

A major goal of the ISS observations at Jupiter was to fill in holes in phase and wavelength of the ring's photometry. Figure 3 shows a plot in 'phase space' of all of the observations of the main ring, including both old and new results. The majority of the existing observations of the ring have been near $\alpha = 180°$ (Voyager, Galileo) where the ring is bright and the planet dark, and near $\alpha = 0°$, where the ring is visible from Earth. All of the Galileo SSI detections used a clear filter, and all of the Earth-based observations have been in the near-IR. Cassini had the opportunity to explore the mid-α portion of the phase curve, and the visible portion of the spectrum. Previous measurements of the spectrum include some Voyager observations, and a spectral cube in forward-scatter by the Galileo NIMS instrument. Recent measurements by Galileo's SSI (Showalter et al., 2001) have filled in portions of the phase curve, including the range $\alpha = 11°$–$45°$ where difficulties with Cassini's attitude control system prevented execution of the planned observations.

We assembled a clear-filter phase curve by combining the normal, radially-averaged I/F values taken during each sequence. The number of frames used per sequence varies; conveniently, the observations with the lowest data quality (the inbound and outbound movies, where the distance from Jupiter was the greatest) also have the largest number of frames, so the error bars for each phase angle are roughly similar. The phase angle is calculated based on the central pixel at the ring ansa.

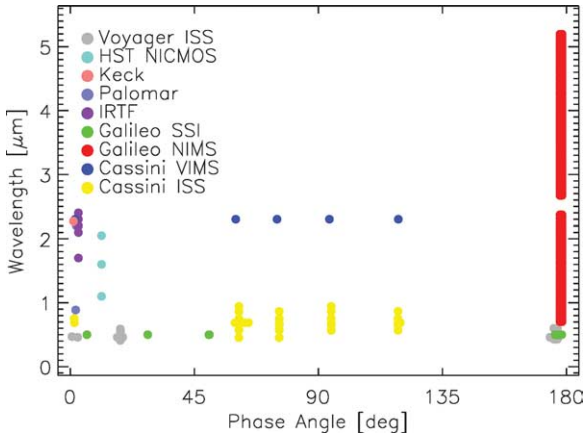

Fig. 3. 'Phase space' of observations of the jovian ring. Cassini's ISS (yellow) and VIMS (blue) have filled in significant regions of phase angle that were previously unexplored. The densest region of points remains a spectral cube of the ring obtained by the Galileo NIMS instrument (red); all Earth-based observations are at the left, at $\alpha < 12°$.

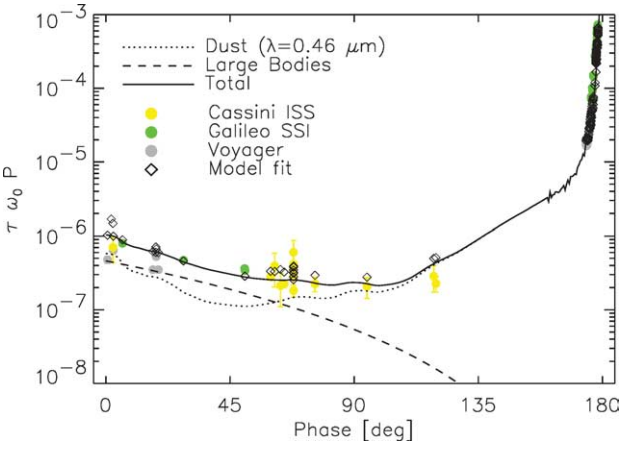

Fig. 4. Clear phase curve. Data points are marked with colored symbols. The three lines are from our best-fit non-spherical particle model phase curve for $\lambda = 0.46$ μm: the dotted line represents the dust component, the dashed line the large-body component, and the solid line the sum of the two. Observations on this plot were taken over a range of wavelengths which vary from that of the lines; therefore, the modeled points (open diamonds) should each be compared to their corresponding data point at the same wavelength, not to the solid line. The small ripples in the dust phase curve are due to the finite number of oblateness values used in our model.

The clear-filter phase curve is presented in Fig. 4. The ring's brightness is generally bounded by that found from the earlier Voyager and Galileo observations. The phase curve is surprisingly flat, varying by only a factor of four between the backscatter and side-scatter (near $\alpha = 94°$). This is significantly flatter than that predicted by a distribution of micron-sized spherical dust grains, which would have a contrast ratio between these phase angles of ~ 50 (e.g., Fig. 15). We will discuss the causes of the phase curve's shape and the fits to the Cassini and other data in Section 4.3.

We have assembled a spectrum in a similar way. Nominally, Cassini's spectral observations included measurements through seven different color filters (Table 2) at each

Table 2
ISS NAC filter combinations used for rings observations

Filter 1	Filter 2	Central λ [nm]	Width [nm]	Notes
CL1	CL2	651.1	340.9	Clear filters
CL1	GRN	569.3	127.0	Green
RED	CL2	648.9	149.9	Red
BL1	CL2	455.5	102.9	Blue
UV2	CL2	306.3	59.9	UV
P0	CL2	633.0	290.4	Clear polarizer
P60	CL2	633.0	290.4	Clear polarizer
P120	CL2	633.0	290.4	Clear polarizer
CL1	IR1	750.1	152.9	Near-IR1
IR2	CL2	861.1	96.9	Near-IR2
CL1	IR3	928.3	66.9	Near-IR3

Central wavelengths have been weighted by the solar flux. The NACs optical path always passes through two filter wheels; at least one of these was set to a clear filter (CL1 or CL2) on all of the observations.

of five phase angles. However, because of the reduced transmission through the spectral filters and the smaller number of measurements at each wavelength, uncertainties in the spectral I/F measurements are large. We observed, however, that the individual spectra at each phase angle are all red with roughly similar slopes (Fig. 5); because of this, we were able to construct a composite spectrum by combining the spectral measurements at all the phase angles into one. We normalized each curve to the I/F at $\alpha = 75°$ before combining them; the error bars are based on the deviations between individual measurements at the same wavelength, and the previously-described calibration uncertainties of the instrument.

The composite spectrum is shown in Fig. 6. The ring is red, increasing in brightness by a factor of 2–3 from 0.45–0.95 μm. This makes it of comparable color to Amalthea (Thomas et al., 1998), Adrastea (Meier et al., 1999), and Saturn's A and B rings (Cuzzi et al., 2002); our measurement is also similar to that of (Showalter et al., 1987), who found a brightening of 1.6–2.0 across the range 0.42–0.60 μm. The jovian rings' red color could be due to light scattered either by a relatively shallow distribution of micron-scale dust grains (e.g., $n(r)\,dr \sim r^{-q}$, $q < 2$) or by macroscopic bodies with an intrinsic red surface color. We model and discuss the source of the ring's color in Section 4.3.

Opposition surge. One of the goals of the inbound movie sequence was to monitor the ring's behavior near $\alpha = 0°$, to see if the ring displayed any evidence for the so-called 'opposition surge' seen on many planetary bodies (e.g., Europa, Helfenstein et al., 1998). The inbound movie monitored the ring continually in the range $\alpha = 0.51°$–$2.51°$.

Unfortunately, accurate photometric measurements on the inbound movie images were difficult for several reasons. First, the stray light was the largest here because Cassini's range to Jupiter ($D \sim 275 R_J$) was the largest, meaning the angular separation between planet and ring was the smallest of the ring observation sequences of the encounter. This decreased the total amount of flux detected from the ring,

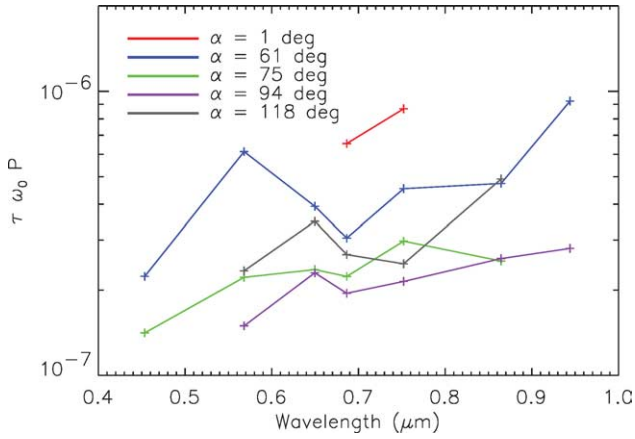

Fig. 5. Cassini ISS observations of the ring's spectrum. The ring's red color is roughly uniform across a wide range of phase angles. A composite mean spectrum from these data points is shown in Fig. 6.

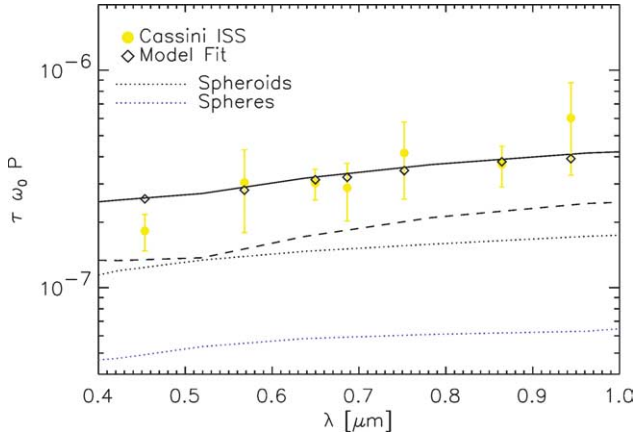

Fig. 6. Composite ring spectrum, for $\alpha \sim 75°$. The ring is red, with I/F increasing almost linearly with wavelength. Symbols are the same as in Fig. 4. In our best fit model, the ring's color is due predominantly to that from the large bodies, suggesting that they must be very red. The dotted blue line (which is a separate calculation for spheres alone) indicates that the spectrum from spherical particles is very similar to that of non-spherical ones.

entrenching the ring deeper into the stray light pattern of the telescope. Several bright 'spikes' of stray light pass directly through the ring, and their changing pattern during this sequence makes their removal difficult. Second, the planet is brightest at low phase angles, increasing its contribution to stray light. Third, these images were short exposures (1.0–2.6 sec), in order to avoid CCD saturation by stray light. Finally, the images were taken using the TABL mode, which compresses 12 bits into 8 using a fixed lookup table. Because the lookup table's spacing is non-linear, this mode had the unfortunate side-effect of substantially reducing our ability to detect the faint ring superimposed on the bright background signal. For these reasons, accurate frame-by-frame photometry of this sequence turned out to be difficult, and it was not possible to observe any opposition surge in the ring. However, by combining the nearly 600 individual measurements, we calculated mean I/F at two wavelengths for

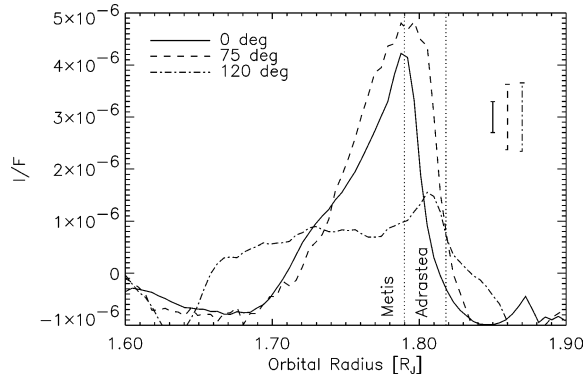

Fig. 7. Radial profiles of the ring. At $\alpha = 120°$, the profile is broad but of low magnitude, consistent with the small particles predominantly seen at forward-scatter. In contrast, the backscatter profiles at $\alpha = 0°$ and $\alpha = 75°$ show the tighter concentration of large bodies toward the ring's outer edge. Error bars for each curve are indicated at the right; errors in orbital radius are approx $\pm 0.02 R_J$.

the entire inbound sequence, with error bars comparable to those of the other sequences.

2.1.2. Radial profiles

We have generated radial profiles based on the sequences at $\alpha = 1°$, $\alpha = 75°$, and $\alpha = 120°$ (Fig. 7). The profiles were created from each image in the sequence by azimuthally averaging the ring pixels in each individual frame. All the individual profiles within the sequence were then combined to create the profiles shown. The ring's well-known 'Metis notch' at $1.79 R_J$ appears in some of the individual radial profiles, but not after they are combined together. This may be due to small errors in our image navigation; therefore, the radial profiles presented here may not represent the full resolution inherent in our data.

The radial profile for $\alpha = 1°$ is sharply peaked at approximately the radial location of Metis ($1.79 R_J$, 127,970 km), and drops to zero inward near $1.7 R_J$ (121,540 km), and outward near $1.83 R_J$ (130,830 km). The side-scatter radial profile ($\alpha = 75°$) is roughly similar. The forward-scatter profile ($\alpha = 120°$), however, is significantly flatter: it does not show a strong peak, but continues inward to near $1.65 R_J$ (117,960 km), and outward to $1.85 R_J$ (132,260 km). We estimate our uncertainties at roughly $0.02 R_J$ (1400 km). The outer edge values we calculate are consistently higher than the Galileo-derived values of $1.805 R_J$ (129,050 km) at low-phase and $1.802 R_J$ (128,800 km) at high-phase Showalter et al. (2001). However, the differences are roughly bounded by the error bars due to the lower resolution intrinsic to our observations.

Differences between the forward-scatter and backscatter profiles have been seen in the Voyager (Showalter et al., 1987) and Galileo radial profiles. The behavior was hypothesized to be due to different populations of particles observed at high- and low-phase. For Galileo observations near $\alpha = 180°$, the ring's brightness comes predominantly from small dust grains, which are often 100 times brighter in forward-scatter than backscatter The dust is easily trans-

ported across the ring or excited in eccentricity, causing its relatively flat radial profile. However, large bodies—which preferentially backscatter—are not as easily transported, and the narrowness of the backscatter profile indicates the narrowness of their present location. (Formally, both the dust and large bodies have equal proportions of flux in their diffraction peaks. However, the large-body diffraction peak is much narrower, and as a practical matter never observed in the visible, so it can be safely ignored.) This explanation fits in naturally with the 'parent body' model by which the large particles produce the small grains through collisions and meteoroid impacts, and the grains are subsequently moved inward by drag forces. Interestingly, the Galileo data show the back-scattered profile to extend further outward than the forward-scattered one, while the Cassini data show the opposite. Although this difference could be significant, it is probably an artifact of the vagaries of stray light removal from the Cassini $\alpha = 0°$ images, and is reflected in the profiles' error bars.

2.1.3. Azimuthal features

Rings contain—as their name implies—more features in the radial direction than the azimuthal. However, azimuthal variations have been detected in the rings of Jupiter and the other planets and we looked for such features in the Cassini data. We first attempted to measure a broad asymmetry between the near–far or east–west arms (first observed by Jewitt and Danielson (1981), and seen in almost all later observations as up to a 50% brightness variation). We also searched for 'clumps' of material in the ring (such as those seen by Showalter (1998) in Saturn's F ring, and by Ferrari and Brahic (1997) in the Encke division); for spokes (such as those commonly observed in Saturn's main rings, Porco and Danielson (1982)); for the 'checkerboard patches' of Ockert-Bell et al. (1999); and for brightness variations fixed in various longitude systems.

The inbound and outbound movie sequences offer an opportunity to monitor the ring for several orbital periods in a roughly fixed geometry. We first inspected every image by eye to look for features, and in particular features that moved in the direction of rotation (as both clumps and spokes would). We did identify a tantalizing sequence of three images (Fig. 8) that appears to show motion of ring material in the keplerian direction. No such features moving in the opposite direction were seen. The low SNR of these images makes identification of any features in this way admittedly quite nebulous, and confirmation that these clumps are real (or not) rests on future detailed analysis. We did not identify any additional structure in the ring such as the checkerboard patches, but this could easily be explained by our lower resolution. The best images for searching for structure are probably those in our $\alpha = 75°$ sequence.

For a more rigorous test, we created azimuthal profiles for all the clear-filter inbound movie frames. These azimuthal profiles indicate the I/F in a pie-slice of the ring, typically in 1° segments of longitude L_S. (Most of the observations

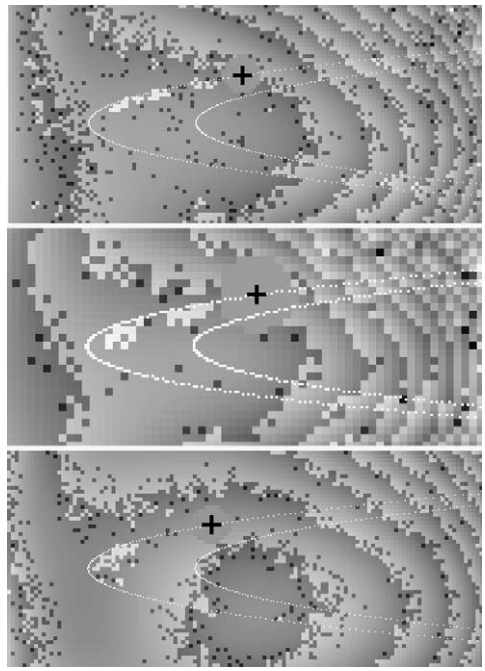

Fig. 8. Possible clumps seen in the ring. This series of three images was taken near $\alpha = 1°$, with a 90-sec delay between the first image pair and a 160-sec delay between the second pair. All images are in the clear filter; the central image was taken in the SUM2 mode causing its larger pixel size. Resolution is 115 km pix^{-1} except for the middle frame, which is 230 km pix^{-1}. The ring boundaries are marked, as is the position of Adrastea (masked out, behind the +). Keplerian motion over this interval would move the clumps $\sim 4°$ in longitude; the ring images span $\sim 40°$ of longitude. The material appears to move in the forward keplerian direction; however, it is difficult to ascertain the clumps' true nature from these images alone.

span about 50° of longitude.) We converted the observations into three different longitude systems, and plotted together all of the observations from the sequence. The three longitude systems were as follows: first, L_S was a solar-referenced longitude with 0° being at the sub-solar point on the rings. Second, we used L_{III}, the System III longitude of Jupiter, which would follow features phased with the Jupiter's internal magnetic field, as has been suggested for Saturn's spokes. Finally, we also converted to $L_{k(R)}$, a 'keplerian longitude' which is constant for a body moving on a circular path at orbital distance R. For this last case, we used values of R in the range 1.65–1.85 R_J, spaced in 0.01 R_J increments.

In none of these coordinate systems did we find any features of interest. A typical plot is shown in Fig. 9. At the level of uncertainty, no clumps are apparent at all. Long-loved features that doubled the brightness over a width of 10° would be visible here, and we can state with certainty that such features do not exist in the data.

2.1.4. Polarization

The ring was observed at polarization angles of 0°, 60°, and 120° during each of the $\alpha = 60°$, $\alpha = 75°$, $\alpha = 94°$, and $\alpha = 120°$ sequences. Polarization could be diagnostic

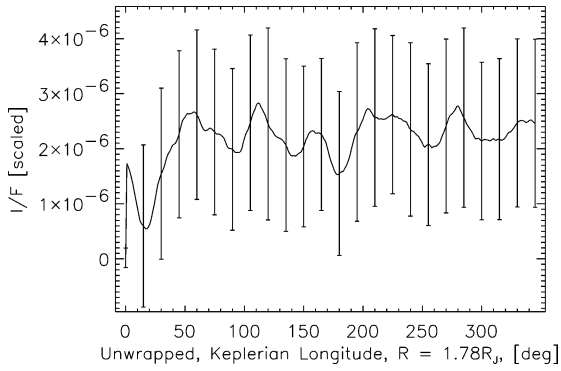

Fig. 9. Asymmetry, keplerian longitude frame, $\alpha = 0°$. This plot represents the brightness of all material moving through the NACs field of view during the 40-hour inbound movie. Longitudes have been converted to a moving coordinate system, so that a moving object would appear as a spike. The dip at 20° is the only feature we found, and is an artifact of the removal of Metis from our images. This plot assumes keplerian motion for $1.78R_J$; not shown are similar plots for 1.65–$1.85R_J$, and for longitudes in the solar and System-III coordinate frames.

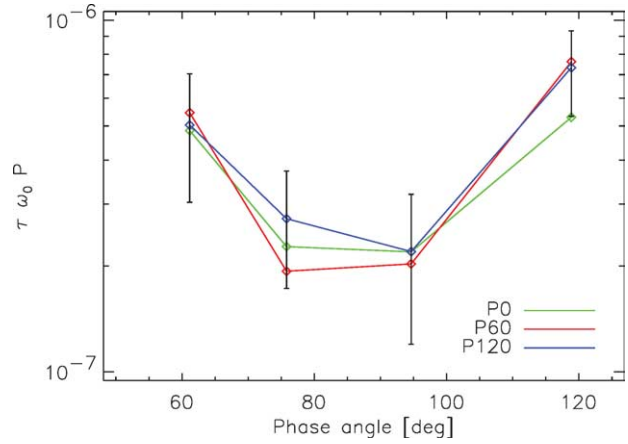

Fig. 10. ISS polarization observations. The ring was observed in a clear filter at three polarization angles, denoted by P0, P60, and P120. Error bars have been taken from comparable non-polarized observations. Because only one frame was taken for each data point, the uncertainty is large and dominates any observable difference at the three polarization angles.

of grain surface structure or grain alignment. Results from these observations are shown in Fig. 10. Unfortunately, each observation consisted of only a single frame and the low SNR in the individual images does not allow us to draw any conclusions from the data at this time.

2.2. Halo and gossamer rings

The halo ring is thought to be composed of dust grains that have been dragged inward from the main ring until they are excited vertically by a Lorentz resonance (Burns et al., 1999; Horanyi and Cravens, 1996). Although the halo's 20,000 km height makes it far thicker than the main ring, its normal optical depth is comparable, suggesting that the same original source region and radial transport processes govern both rings.

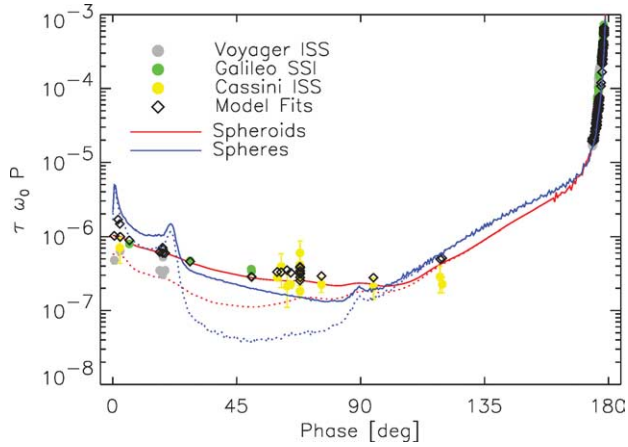

Fig. 15. Comparison between the phase curves for spherical and non-spherical grains. Symbols are the same as in Fig. 4. Both phase curves are best fits; their actual size distributions differ slightly, as described in the text. For clarity, the curves for large grains are not plotted, although they are included in the models. The non-spherical-particle phase curve (red lines) is flatter in mid-phase observations; the spherical grains reflect too-little light at mid-phase to match the data. Also, the non-spherical grains better match the flat response toward $\alpha = 0°$. Forward-scattered diffraction is indistinguishable between the two particle types.

We were unable to detect the halo ring in any of our images. This was not surprising, for several reasons. First, because the halo is vertically extended, it does not brighten as dramatically as the main ring for low elevation angle B. In Cassini's viewing geometry, geometric effects alone would predict the halo to be 10–100 times fainter than the main ring. Second, the halo resides entirely inward of the main ring, and thus sits even deeper within the stray light of Jupiter. It is possible that extensive processing of our images may uncover the ring, in much the same way that Showalter and Cuzzi (1993) were able to detect Saturn's G ring by summing pixels within the ring's known boundary, though the ring could not be seen in the data by simple inspection. We leave such analysis to a future party.

We also searched for signatures of the 'gossamer' rings, particularly in the region surrounding and outward of the Thebe ring (at $3.1R_J$, with thickness ~ 4400 km and $\tau \sim 10^{-7}$ (Burns et al., 1999)). We searched for gossamer material in 15 NAC frames taken outbound from $247R_J$ at $\alpha = 118.5°$. The observations, arranged in a 1×3 mosaic along the ring plane, searched the region from $3.04R_J$ to $7.62R_J$. The exposures ranged up to 100 sec in a variety of filters. To seek this material, we summed wide swaths of pixels in the vertical and radial directions, searching in particular for vertically-symmetric features that corresponded to the known position of the Thebe ring. In none of the images did we detect this ring or any other known or unknown ring material. We place an upper limit for material in this region of $I/F < 3 \times 10^{-7}$. Our sensitivity was limited by dark-current calibration of the NAC detector and by the 2-Hz banding structure of the ISS electronics; stray light from Jupiter was not significant for these images. It is possi-

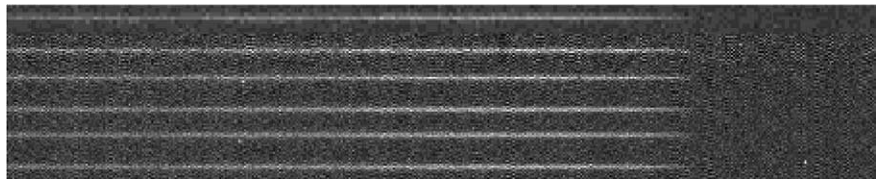

Fig. 11. The ring's right ansa, as seen in five images taken at an elevation $B = -0.03°$. As shown in Fig. 13, these images show only the ring's near arm. The five clear-filter images have exposures of 1.5–18 sec, and span a total of ~ 5 minutes. The top image has been resampled from the lower SUM2 resolution; the checkerboard patterns in the bottom images is an artifact of our dark-current subtraction.

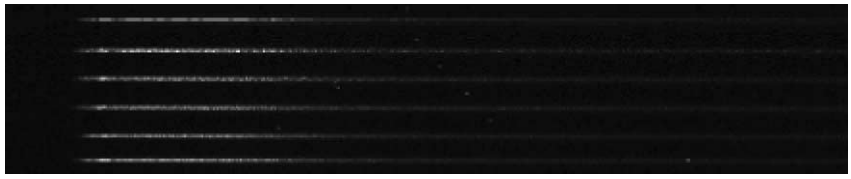

Fig. 12. The ring's left ansa, at $B = -0.02°$. In contrast to Fig. 11, these images include the fully-lit near and far arms. The object moving through the images is a background star. Small apparent 'bumps' can be seen several pixels inward of the ansa at $\sim 1.72 R_J$ (left side of image). The image has been stretched to enhance contrast.

ble that with improved dark-current calibration, comparably faint rings could be observable at Saturn.

Because the Thebe ring is much more vertically condensed than the halo, we were initially surprised to not detect it. Like many surprises it can be easily explained in retrospect. Assuming that the gossamer material is dominated by 5-μm particles (Burns et al., 1999), Eq. (1) predicts $I/F \sim 10^{-6}$–10^{-7} for this observing geometry. The rings were easily detected by Galileo; however, this was due largely to the forward-scattering geometry ($\alpha \sim 178°$) of those observations, as the phase function of grains this size increases by 10^3–10^5 as the observer moves toward forward-scattering. We calculate that for a ring of $\tau = 10^{-7}$, submicron-sized grains, 5-μm grains, and large macroscopic bodies all have comparable visibility at Cassini's observing geometry. Therefore, in hindsight the ring is very difficult detect at $\alpha = 120°$ regardless of its makeup.

2.3. Ring plane crossing

Cassini observed the ring immediately after passing through the ring plane from above. Intended to probe the ring's vertical structure, the observations included six exposures on the ring's left ansa ($B = -0.02°$, $\alpha = 63.3°$, Fig. 11) and six on the right ($B = -0.03°$, $\alpha = 64.6°$, Fig. 12) taken 30 minutes later. Because the ring-plane crossing (RPX) corresponded roughly with closest approach, the spatial resolution of 59 km pix^{-1} is nearly the highest seen in the observations. RPX is also where the deepest images of the ring were taken, including 5.6, 8.2, and 18–32 sec full-resolution images of each ansa. Furthermore, because at RPX the ring's light is spread amongst many fewer pixels in the vertical direction stray light removal is far easier. All of the images were taken through the clear filters.

Fig. 13. The geometry of the encounter during the ring plane crossing sequences. In this diagram, the spacecraft approaches from below, and passes to Jupiter's right. The lit face of Jupiter points toward the Sun, with phase angle $\alpha = 64°$. The grey bands indicate the lines-of-sight for observations of the left and right ansa during the ring plane crossing. The right ansa was partly in shadow, while the left ansa was fully-lit. Jupiter polar image from Porco et al. (2003).

Cassini's phase angle of $\alpha = 64°$ dictated that the ring's left[3] ansa was fully lit, but the right ansa was less than half lit (Fig. 13). This allows us to probe the ring's front and back arms separately, but does make comparison between

[3] By 'left,' we will always be referring to the ansa as viewed by an observer standing on the Sun's north pole. To confuse matters slightly, observations of the ring's left ansa at RPX were erroneously given the sequence name RPLNXNG_PRIME_RIGHT_B, and vice-versa for the right ansa.

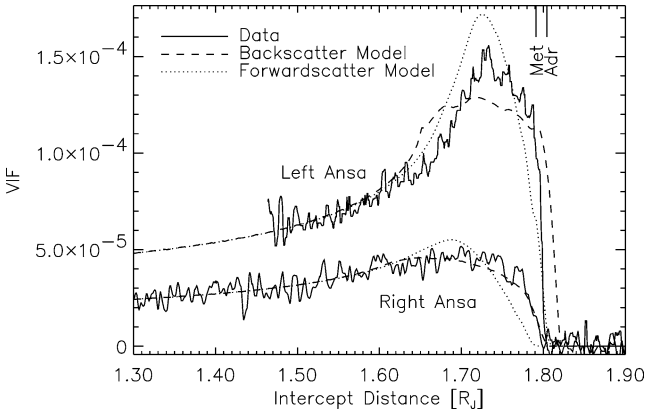

Fig. 14. Radial scans of the ring's left and right ansa, taken during the ring plane crossing. The dotted and dashed lines are modeled values of the radial scans, based on the known intrinsic radial profile of the ring in backscatter (dotted line) and forward-scatter (dashed line). The data generally lie between these two extremes, as would be expected at $\alpha = 64°$, indicating that even at this phase angle, roughly comparable amounts of light are scattered from both large and small particles. The good overall model fit indicates that the apparent difference in brightness between the two arms can be explained entirely by geometrical effects, and not an intrinsic asymmetry in the ring.

the two ansae somewhat more involved. Note that only during the RPX did Cassini make substantial observations of both ansae; these are therefore the best data of the encounter to look for large-scale asymmetries.

Figure 14 shows the observed radial scans of the left and right ansae. (We use 'radial scan' for the edge-on observation along a line-of-sight, and 'radial profile' for measurements of the actual amount of material at each orbital distance.) The left ansa's peak brightness is approximately three times that of the right. It was necessary for us to do some modeling in order to determine whether the observed asymmetry was intrinsic, or can be explained by simple geometric effects associated with the difference in solar illumination between the left and right ansae. In order to do so, we created a 2D model of the ring, and summed the amount of lit material seen along each line-of-sight. This allows us to create a model edge-on 'radial scan' of the ring, using an assumed radial profile. We used radial profiles of the ring taken by Galileo (S. Brooks, unpublished, 2003); these data are of higher resolution than the Cassini profiles described earlier.

Our models match the radial scans very well; in particular, the magnitude of the observed left-to-right asymmetry is matched flawlessly, indicating that we see no intrinsic brightness difference (at the 10% level or better) between the two ansae. This is consistent with our earlier results (Section 2.1.3) where we are unable to detect any asymmetry in the ring. Brooks et al. (2003) explores various options for the ring's asymmetry and concludes the most likely to be stochastic dust-releasing collisions within the ring. These collisions are still rare, however, and our lack of asymmetry is hence perhaps not surprising.

The scans also yield information about the particles' radial distribution. The plot shows model radial scans based on radial profiles taken in backscatter (dominated by macroscopic bodies) and forward-scatter (dominated by dust), alongside the observed scans. The latter appear to be roughly bounded by these two models; in particular, the left ansa data suggest the observed ring extends farther out than the forward-scatter profile shows, but has a sharper peak than the backscatter scan. This is almost certainly due to the fact that the ring at $\alpha = 64°$ in fact *is* composed of comparable flux from both large and small particles (e.g., Fig. 4).

Images of the ring's fully-lit left arm appear to show small, elongated 'bumps' of approximately 3×1 pixels in the ring plane, near the ansa at $1.72–1.73 R_J$ (Fig. 11). The bumps are well-defined, and approximately 20% brighter than the ring material immediately surrounding them; no such brightenings were observed on the right ansa. They are compact enough that we originally identified them as satellites in the ring plane. However, we did not measure any appreciable motion of the bumps during the 5 minutes we observed the ansa; we calculate that a keplerian body *on the ansa* at $1.72 R_J$ would move ~ 3 pixels (4.5° of longitude) during the 5 minutes of observing, and we could have detected this motion. The bumps are not due to any known satellite, and stars in the field move dozens of pixels during the sequence due to spacecraft motion. We also eliminated CCD artifacts as a possible source: the features appear in the same place on the ring in every image, even though pointing jitter caused a 2–3 pixel variation in the ring's positioning on the CCD throughout the sequence. (Error in the spacecraft's tracking is more evident in these 5-minute sequences than in the much-shorter individual exposures.)

We offer two possible explanations for these bumps. First, they may be due to a slight density variation at that position of the ring—i.e., an intrinsic clump of material. Such a density variation could have no apparent motion if it were an arc-like feature spanning perhaps 10° in latitude ($\sim 20{,}000$ km). Possible clump-like features have been reported before (e.g., the checkerboard patterns of Ockert-Bell et al., 1999). However, a more prosaic explanation may be that the observed bumps are no more than a natural consequence of a particularly long line-of-sight at $1.72 R_J$ looking along the ring's intrinsic radial profile. Indeed, the bumps' radial location is well-predicted by the model radial scan (Fig. 14). The fact that the right ansa lies partly in shadow makes its peak more subdued. We mention the possibility of clumps more as a footnote; because of the unique geometry and high spatial resolution, this is indeed the first time that such features (whatever their source) have been observed in Jupiter's ring.

The RPX observations can also be used to constrain the ring's vertical thickness. Previous observations have determined a 300 km upper limit in forward-scatter and 30 km in back-scatter (Showalter et al., 1987), while Galileo data at $\alpha = 98°$ inferred a thickness of ~ 100 km (Ockert-Bell et al., 1999). The ring's possible greater thickness at forward-scatter is consistent with the notion that vertically extended dust is responsible for most of the forward-scattered light,

and larger bodies which are less easily excited are seen in their flatter orbits at backscatter.

We computed the ring's thickness by directly measuring the FWHM of the ring's brightness profile in the vertical direction, using a single 32-sec exposure. We radially summed local areas of the ring image, and fit gaussians to these profiles to determine the ring's FWHM thickness. The ring's projected thickness increases in the direction toward the planet, from a FWHM of 80 km at $1.75 R_J$, to 160 km at $1.55 R_J$. This degree of thickening (which is not visible to the eye in the images) is consistent with that expected from a thin ring observed at $B = 0.03°$. To estimate our resolving limit, we located a field star of similar brightness that had been smeared by the spacecraft's motion (parallel to the ring plane) during the long exposure. The 'thickness' we measured of this star trail using the same method was ~ 80 km. The ring at its thinnest is therefore essentially indistinguishable in profile from that of a point source, and we place a limit on its intrinsic thickness in a side-scattering geometry of FWHM $\lesssim 80$ km at $\alpha = 64°$, consistent with the 100-km full side-scattered thickness derived from Galileo images. Based on our photometric model (e.g., Fig. 4), we believe that the ring at this phase angle is visible through roughly equal contributions from small and large particles—in fact, in almost the same ratio as at the Voyager backscatter observation at $\alpha = 0°$–$2°$.

3. Previous observations

The past quarter-century has seen nearly fifteen separate observing programs targeted at the ring. In this section, we will describe these observations. In Section 4 we will use the new ISS data in conjunction with the existing data sets to leverage the power of wide coverage in phase angle and wavelength that comes from the many different observations. Before describing the data, we first detail the photometric quantities which we will examine.

We are interested primarily in observations of the radially-averaged normal I/F of the ring, that is,

$$\left(\frac{I}{F}\right)_{\text{rad}}(\lambda,\alpha) \equiv \frac{EW}{\Delta R} \equiv \frac{1}{\Delta R}\int \frac{I}{F}(R,\lambda,\alpha)\,dR. \qquad (2)$$

The 'equivalent width' EW has units of length. ΔR is the ring's width, which we take to be 6500 km. I/F is the normal reflectance of the ring, where I is the intensity measured at the detector, and πF is the incident solar flux. I/F of a Lambertian surface is thus 1. Unless otherwise mentioned, we use the normal I/F, which removes the simple geometric differences of looking through different path-lengths of ring material due to a non-zero emission angle. The normal I/F is thus not an observed quantity, but a useful quantity for comparison.

3.1. Data sets

We here examine particulars of the various data sets. There are significant differences in the programs that often make comparing different data sets challenging. With all of the previously-reported observations we include here, we have not re-calibrated the observations either radiometrically or spectrally, but use their published values and errors. *However, we have in several cases* (*described below*) *scaled the* I/F *to adjust for differences in viewing geometry.*

3.1.1. Voyager (1980)

After Voyager 1 discovered Jupiter's ring system with one 11-minute exposure, Voyager 2 followed up and took 24 additional images. Voyager 2's images were taken through its clear, violet, orange, and green filters, at phase angles of 3°, 16°–19°, and 173°–177° (Fig. 3). These images were analyzed by Showalter et al. (1987), who presented the ring observations in units of radially-averaged normal $\tau\varpi_0 P(\lambda,\alpha)$. Calibration and reduction uncertainties in the Voyager's vidicon detector caused up to a 50% in the absolute scaling of their results, although the relative calibration between different images was 5–10%. Real variations in brightness between the ring's near and far arms contributed an additional $\sim 10\%$ scatter to their results. In many cases, however, they were able to measure the ring's brightness over a range of phase angles within the same image, and a consistent phase curve can be constructed piece-wise from these segments, even if the segments do not match in absolute calibration. We have taken the Voyager data and error bars as presented in their Figs. 4.3 and 4.4.

3.1.2. Palomar & IRTF (1980)

Early ground-based observations of the ring were made by Neugebauer et al. (1981), who used a CCD on the Mt. Palomar 5-m telescope to image the ring at $\lambda = 0.887$ μm and $\alpha = 1.9°$. Several days later, the same group used an InSb photometer on the NASA Infrared Telescope Facility (IRTF) to perform aperture photometry on the ring at five wavelengths between 1.7 and 2.4 μm, at a phase angle $\alpha = 2.9°$. In both cases the ring was within 1° of edge-on. The observations, reported in terms of vertically-integrated magnitudes per linear arcsec, showed the ring to be red and increase in brightness by a factor of 2.5 across their wavelength range.

In light of current knowledge of the ring, these results must be interpreted carefully. The Palomar observations (at 0.887 μm) were made by summing flux at an intercept distance 1.48–$1.81 R_J$, while IRTF (at 1.7–2.4 μm) used an aperture placed at 1.42–$1.68 R_J$. Although Neugebauer et al. (1981) corrected for the different *sizes* of the apertures, the difference in each aperture's *position* caused the Palomar observations to be taken looking through substantially more ring material than the IRTF observations.

Our model of edge-on line-of-sight path lengths (Section 2.3) can be used to correct for these differences. Using

this model, we calculate that the relative IRTF brightnesses should be increased by ∼ 30% in order for the Neugebauer et al. (1981) spectrum to accurately reflect the ring's intrinsic color. This correction increases even more the already very red color indicated by their results.

3.1.3. Palomar (1988)

Nicholson and Matthews (1988) used the Palomar 5 m telescope to measure the ring's brightness at wavelength $\lambda = 2.2$ μm, phase angle $\alpha = 2.2°$, and a ring opening angle of 3.2°. They found a mean normal ring brightness $\tau\varpi_0 P = 1.7 \times 10^{-6}$. Because of non-photometric conditions, their measurement was calibrated relative to Amalthea rather than standard calibration stars.

3.1.4. Keck (1997)

During the August 1997 jovian RPX event, de Pater et al. (1999) imaged the ring from the 10 m Keck telescope at 2.27 μm. The opening angle was 0.17°, and phase angle $\alpha = 1.1°$. Because these observations were taken edge-on, the direct results are radial scans (their Fig. 3, akin to our Fig. 4). To invert these to a generalized normal brightness that could be compared to non-RPX measurements, the authors used their so-called 'onion-peeling' method of linear differentiation, resulting in vertically-integrated I/F radial profiles (their Fig. 6, dashed line). We use their radial profile to calculate a mean normal $I/F = 3.5 \pm 1 \times 10^{-7}$ (i.e., $\tau\varpi_0 P = 1.4 \pm 0.4 \times 10^{-6}$) for their data.

To verify our own method of radial profile scan inversion, we applied our technique to the Keck radial scans in the same way we did so for the IRTF data. This gave us a mean normal $I/F = 5.0 \times 10^{-7}$, a reasonably good agreement to de Pater et al. (1999) considering the noise inherent in the data.

3.1.5. HST NICMOS (1997)

HSTs NICMOS camera was used by Meier et al. (1999) to image the ring in the infrared at $\lambda = 1.1$, 1.6, and 2.05 μm during the fall 1997 jovian ring-plane crossing event. The phase angle was $\alpha = 11.3°$, and the ring opening angle was 0.06° (< 1 pixel). To invert their results to a generalized normal brightness that could be compared to non-RPX measurements, the authors used a radial profile model similar to ours to remove the line-of-sight effects from their results. They presented their final, de-projected main-ring spectrum in terms of vertically-integrated μJy per linear arcsec, rather than I/F. Although they note that their final brightness matched well that of the Keck observations, this is unlikely to be significant because the wavelength, phase angle, and Earth–Jupiter distance were substantially different between these two observations.

3.1.6. Galileo SSI (1996)

Galileo's Solid-State Imager (SSI) was used to take eight clear-filter images of the ring system during the spacecraft's C3 orbit of Jupiter. The ring was close to edge-on ($B =$ 0.46°), but well-resolved due to the spacecraft's proximity to Jupiter (∼ $32R_J$). Phase angles ranged from $\alpha = 175°$–179°. The observations are described extensively in Ockert-Bell et al. (1999) and Burns et al. (1999). Recent work by Brooks et al. (2003) complements the earlier studies by examining the phase curve of the data and constraining the size distribution of the dust responsible for the forward-scattered light. This latter work presented photometric results in terms of radially-averaged normal $\tau\varpi_0 P$, in much the same way as earlier Voyager results.

3.1.7. Galileo NIMS (1996)

Concurrent with Galileo's visible observations, the spacecraft's Near-Infrared Mapping Spectrometer observed the ring from the same geometry during the C3 orbit. McMuldroch et al. (2000) analyzed the cube of data returned, and produced spectra of the ring from 0.7–5.2 μm, at each of four radial intercept distances. Brooks et al. (2003) re-analyzed the NIMS data, improving the navigation and data reduction, and fitting a particle size-distribution to the data. Brooks et al. (2003) produce results in units of normal I/F (their Fig. 6), which we use here. We note that they fit $n(r)$ distributions to the visible phase curve and the four infrared spectra; however, they did not attempt to fit these five data sets simultaneously.

3.1.8. Cassini VIMS (2000–2001)

The Visual and Infrared Mapping Spectrometer (VIMS) onboard Cassini shared many ring observations with the ISS. Both instruments are mounted directly to the spacecraft assembly, and their fields of view are nearly aligned. ISS and VIMS observed together at the $\alpha = 0°$, 60°, 75°, 94°, and 120° opportunities. The VIMS observations differed from the NAC ones in that VIMS has a much lower spatial resolution (500 μrad vs. 6 μrad), but images each pixel in up to 352 spectral channels in the range 0.3–5.2 μm.

Based on the VIMS observations, Brown et al. (2003) presented a phase curve of the ring in terms of vertically-integrated I/F (VIF) at five phase angles. Stray light and the instrument's intrinsic resolution made the data reduction challenging, and the ring was detectable only after summing several hundred individual images. Although the VIMS data span their entire wavelength range, stray light was lowest near $\lambda = 2.3$ μm and only these observations have been published to date.

The VIMS observations can be considered 'edge-on' due to the spatial resolution intrinsic to the instrument. The VIF values presented by Brown et al. (2003) are averaged over the radial intercept range 1.40–1.68R_J. In order to compare these to normal I/F values, the VIFs must be adjusted downward to compensate for the line-of-sight path length intrinsic to the VIMS observations. Using again the methods in our Section 2.3, we calculate a line-of-sight correction factor of 4.6 (including a factor of 2 to account for both arms), and have divided their I/F values by this factor to compensate

for their pathlengths. We then converted from VIF to normal I/F by dividing out the ring's assumed radial width.

Brown et al. (2003) compared their results with those taken with Keck, NICMOS, and Palomar/IRTF, by converting the latter observations' brightnesses (in magnitudes per linear arcsec) to VIF widths. However, the values as plotted in their paper were not adjusted for the change in Earth–Jupiter and Sun–Jupiter distances, causing the HST and Palomar/IRTF data points to be erroneously low by 15–20%.

3.1.9. Cassini ISS (2000–2001)

A fit to the ISS phase curve, assuming a combination of non-spherical small particles based on the Mishchenko and Travis (1998) model and larger parent bodies, was presented by Porco et al. (2003). Since publication of that report, we have improved the calibration of the phase curve, and added spectral observations and the studies of the ring's morphology which we address in this paper. We have also substantially improved our particle model; the one in Porco et al. (2003) considered only one shape model, not the ensemble of shapes that we describe in Appendix A.

3.1.10. Other observations

Additional early ground-based observations of the ring were reported by Becklin and Wynn-Williams (1979) and Smith and Reitsema (1980). Observations of the ring with the IRTF during the Shoemaker–Levy/9 impact were reported by Orton et al. (1995) but these data have not been reduced; some additional Keck observations also await reduction (de Pater, personal communication, 2002). Galileo's Ultraviolet Spectrometer (UVS) failed to detect the ring in an observation during orbit C9 (Throop, personal communication, 1998). Recent observations of the ring during the 2002–2003 ring plane crossings were made by Showalter et al. (2003) using HSTs Advanced Camera for Surveys (ACS) and de Pater et al. using Keck, and we look forward to their results.

4. Size distribution and physical properties of ring particles

4.1. Light scattering

In a low optical depth ring such as Jupiter's, the $I/F(\lambda,\alpha)$ can be related to the particle distribution by way of

$$4\mu\frac{I}{F} = \tau\varpi_0 P(\alpha) = \int n(r)\pi r^2 Q_{\rm sca}(r)\,P(r,\alpha)\,dr, \qquad (3)$$

where $n(r)$ is the vertically integrated differential particle size distribution. Computing the I/F for a given distribution of particles is a matter of computing values for the scattering efficiency, $Q_{\rm sca}$, and the phase function, $P(\alpha)$. A value of $Q_{\rm sca} = 1$ (which is the norm for bright macroscopic particles at backscatter) indicates that the particle's scattering and geometric cross-sections are identical. The quantity ϖ_0 is the particle's single scattering albedo, and for large particles ϖ_0 is the same as the Bond albedo. The phase function, $P(\alpha)$, describes the directionality of light scattered from a particle and is normalized such that

$$\int_0^\pi P(\alpha)\sin(\alpha)\,d\alpha = 2. \qquad (4)$$

The ring is probably composed of at least two distinct types of particles (e.g., Showalter et al., 1987). Most of the light—especially in forward-scatter—comes from small dust grains, with sizes up to perhaps tens of microns. Because of the complex way that the small-particle scattering depends on input parameters, the resultant $I/F(\lambda,\alpha)$ depends predominantly on the particles' size distribution, rather than their composition.

The traditional way to compute P and Q for these particles is with *Mie* scattering (e.g., Bohren and Huffman, 1983). We also use a non-spherical particle model (Mishchenko and Travis, 1998) which computes the scattering coefficients for wide range of oblate spheroids, and has been shown to more accurately model light scattering from many particles found in nature (Mishchenko et al., 1997). There have been a few elementary applications of non-spherical particles to planetary rings in the past (e.g., Throop and Esposito, 1998; Showalter, 1996; Showalter et al., 1992); the latter models were based on a semi-empirical model for scattering from cubes developed by Pollack and Cuzzi (1980). Porco et al. (2003) applied a sophisticated non-spherical particle model to rings, based on a range of oblate spheroids Mishchenko and Travis (1998). The model presented here improves on our earlier work by considering an ensemble of spheroidal shapes, rather than just a single shape of spheroids; we also significantly extend the size range of the largest spheroids. The details of our particle model are described in Appendix A.

In contrast to dust, large bodies (macroscopic or 'parent bodies' of perhaps mm- to km-sizes) scatter light in ways similar to those of large bodies on Earth. Their brightness decreases smoothly from backscatter to forward-scatter, and their spectrum is essentially independent of viewing geometry. For this work we adopt the spectrum of the Trojan asteroid Hektor (Cruikshank et al., 2001) and the phase curve of Callisto (Squyres and Veverka, 1981). Hektor was chosen because it has a smooth red slope with few features from 0.3–3 μm. The particular choice of phase curve makes little practical difference in the fit; the effect of the spectrum is discussed in Section 4.3.

Combining the large and small particles, and defining their optical depths as τ_l and τ_s, respectively, we can write Eq. (3) as (e.g., Throop and Esposito, 1998):

$$\tau\varpi_0 P(\alpha,\lambda) = \tau_s\varpi_{0,s}P_s(\alpha,\lambda) + \tau_l A(\lambda)P_l(\alpha). \qquad (5)$$

Using Eq. (3) for small particles, the above equation becomes:

$$\tau\varpi_0 P(\alpha,\lambda) = \int_{r_1}^{r_2} n(r)\pi r^2 P(\alpha,\lambda,r) Q_{\rm sca}(\lambda,r)\,dr + \tau_l A(\lambda) P_l(\alpha), \quad (6)$$

with

$$\tau_s \equiv \frac{\int_{r_1}^{r_2} n(r)\pi r^2 P(\alpha,\lambda,r) Q_{\rm sca}(\lambda,r)\,dr}{\int_{r_1}^{r_2} P(\alpha,\lambda,r) Q_{\rm sca}(\lambda,r)\,dr}, \quad (7)$$

where r_1 and r_2 denote the boundaries of integration for the small grains. Values of P outside the integrals refer to the ensemble phase functions, while those inside depend on the particle size.

4.2. Fitting procedure

Together the jovian rings observations over the last 25 years comprise approximately 1500 data points of $I/F(\lambda,\alpha)$. This number is somewhat arbitrary; for instance, many Voyager images contribute several points in phase angle across their frame, while the hundreds of images from the Cassini inbound movie are summed into just one VIMS and two SSI data points. Alternate methods of data reduction could result in different numbers of final data points.

Given these datapoints, it was our objective to determine $n(r)$. To address the problem, we quantized $n(r)$ into ~ 100 size bins across the size range $r = 0.01$–100 μm. Additional free parameters include τ_l and τ_s. The spectrum assumed was that of the Asteroid Hektor (Cruikshank et al., 2001), with a phase curve of Callisto (Squyres and Veverka, 1981). The refractive index of the small particles was fixed at $1.5 + 0.001i$, typical for silicates; however, the results are relatively insensitive to this value.[4]

Many methods can be used to determine the best-fitting parameters to fit a data set. We first attempted an automated root-finding routine, using a standard non-negative least square approach (the IDL `LMFIT` routines of C. Markwardt, based on the standard `MINPACK-1` algorithms). Our goodness-of-fit was judged by a standard χ^2 sum over all the data points, weighted by the appropriate error bars.

The large number of free parameters ($N > 100$) and the simplicity of our goodness-of-fit metric made it difficult to converge to a solution. Although McMuldroch et al. (2000) found success with an automated method, we were unable to do so ourselves. We simplified the problem significantly by reducing the number of parameters describing the small-particle size distribution. We chose a two-component power-law distribution, which Brooks et al. (2003) found to offer significantly better fits than the standard single-component power laws. Our distribution then takes the form

$$n(r)\,dr = C_1 r^{-q_1}\,dr \quad \text{for } r < r_b, \quad (8)$$

$$n(r)\,dr = C_2 r^{-q_2}\,dr \quad \text{for } r \geqslant r_b, \quad (9)$$

with the constants C_1 and C_2 set such that $n(r)$ is continuous at the breakpoint r_b. The number of parameters then reduces to five: τ_s, τ_l, q_1, q_2, and r_b.

Even with this reduction in parameter space, lengthy experiments with the `LMFIT` routine indicated that the five parameters still affect χ^2 in a complex-enough way that automated root-finding routines, although they converged to a local minimum, were not going to be successful in finding global minima. We therefore decided to fit the three 'shape' parameters (q_1, q_2, and r_b) by manual iteration. Then, optical depths τ_l and τ_s could easily be fit automatically because they are simple linear coefficients.

The observed I/F data points are each functions of λ and α, and can therefore not be visualized on a single plot, as a simple phase curve or spectrum. However, various subsets ('slices') of the data can be easily plotted. We chose five of these (a phase function in the visible and infrared, and spectra at low, intermediate, and high phase angles) to examine manually as we varied parameters to converge on best-fit solutions.

We found that it was not possible to fit the absolute magnitude of all data sets simultaneously. In order to fit the visible and IR phase curves simultaneously, we were forced to scale all of the VIMS data downward by a factor of 0.4. Similarly, the NICMOS data were forced to be scaled up by 1.5. These scalings preserve the *shape* of the spectra and phase features, and change only their magnitude. We were puzzled and concerned by the need for scalings of this magnitude, which exceeded both the noted asymmetry in the rings and the uncertainty of the measurements. Notably, however, the visible-light Voyager, Galileo, and Cassini data needed no scaling amongst themselves; these three data sets are the most similar in means of acquisition. Given the ring's extreme subtlety and its often marginal detection, we believe that the absolute calibration of the VIMS and NICMOS data sets appears inconsistent.

4.3. Particle size distribution and composition

We have determined best-fit solutions for the ring for the two models. For both the spherical and non-spherical particle models, we find $q_1 = 2.0 \pm 0.2$, $q_2 = 5.0 \pm 1$, $r_b = 15 \pm 0.3$ μm. For the non-spherical case, we find $\tau_l = 4.7 \times 10^{-6}$ and $\tau_s = 1.3 \times 10^{-6}$, while for spheres our best-fit solution is $\tau_l = 7.0 \times 10^{-6}$ and $\tau_s = 1 \times 10^{-6}$. Both of these distributions have a peak of $r^2 n(r)$ (that is, the largest contribution to surface area) near 15 μm, a similar result to that found by McMuldroch et al. (2000) and Brooks et al. (2003). The source of this peak is undetermined. However, Brooks (2003) has shown that dynamical interactions with

[4] Showalter et al. (1987) used an imaginary component of $0.01i$; our lower value is in part required for numerical efficiency of our non-spherical particle calculations, and for consistency we use the same for spherical particles as well.

Metis may cause some grains to be slowed as they cross the ring, thus increasing their number density. Further modeling could indicate the viability of this process and its effect on the size distribution.

It is significant that we are able to fit the piece-wise *shapes* of both the phase and spectral observations with one unified size distribution. This suggests that, first, our size distribution is probably quite accurate; and second, even though processes in the ring may operate on timescales as fast as hours according to some models (Horanyi and Cravens, 1996), the overall bulk properties of the ring have not changed over the last two decades.

4.3.1. Fits to phase curve

Our best fit to the visible phase curve is shown in Fig. 4. The phase curve is a sum of the components from large and small bodies. In forward-scatter the ring is visible only through its dust; in backscatter, the dust and large bodies contribute similar amounts of flux. Because these two components have opposite dependences on α, the phase curve remains flatter than either of them alone over most of the range $\alpha = 0°$–$120°$. We find that the overall optical depth is dominated by large particles, not dust. Showalter et al. (1987) concluded that optical depths of 1×10^{-6}–6×10^{-6} for each component fit the Voyager observations; our results are consistent with these and better constrain them.

Non-spherical particles fit the data significantly better than the spheres (Fig. 15). This is particularly evident near backscatter (where the spheres show too large a 'glory' peak) and in side-scatter (where the spheres drop too low in brightness). The non-spherical grains scatter more isotropically than spheres. This behavior has been previously noted in the F ring (Showalter et al., 1992) and the A ring (Dones et al., 1993). In the second study, the authors introduced isotropic particles of $r = 10$–100 μm in Saturn's A ring to fit its observed phase curve. They justified these particles' phase function based on measurements of rough and 'fluffy' interplanetary dust particles, which showed them to scatter nearly isotropically. Later, Throop and Esposito (1998) also used isotropic particles to fit observations of Saturn's G ring; such particles could be formed of amorphous ice and include numerous small voids, which would cause a strong trend toward isotropic scattering (McGuire and Hapke, 1995; Mishchenko and Macke, 1997). Our scattering model cannot distinguish between the effects of particle shape and the effects of inclusions and fluffiness (causing isotropic scattering); however, we can definitively say that homogeneous spherical particles do not fit the data. It would indeed be surprising if the grains were found to be homogeneous spheres; certainly, collisions and environmental processing contribute to both making the particles non-spherical and modifying their scattering behavior. It is unlikely that the true nature of the particles can be better constrained by continued remote sensing observations; in situ sampling of the dust would allow for much greater understanding of its properties and histories.

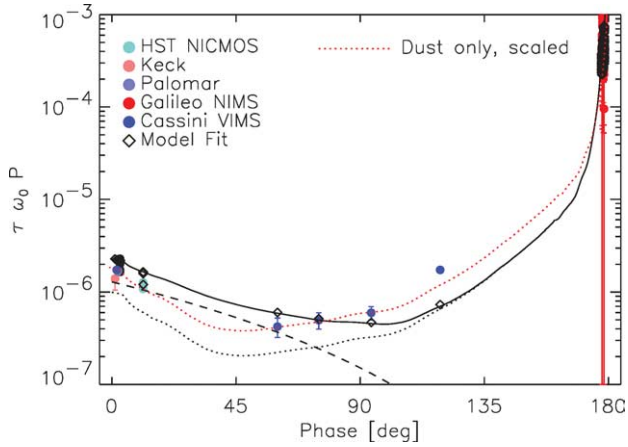

Fig. 16. Infrared phase curve for data points with $\lambda = 1$–2.5 μm. Symbols are the same as in Fig. 4. The best-fit model provides only a fair fit to the VIMS data. However, the phase curve of the dust alone (red curve) matches quite well, suggesting that the large bodies could be quite dark at the $\lambda = 2.3$ μm wavelength of the VIMS observations.

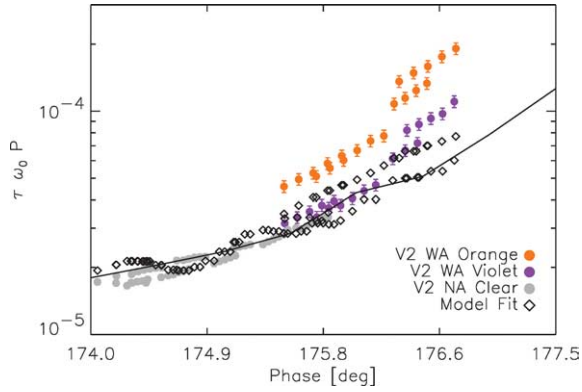

Fig. 17. Phase curve of Voyager observations. Our solution fits the slope of each segment; variations in the offset between different images are due to in part to calibration uncertainties near image corners in the Voyager observations, and in part to actual differences in the near and far arms of Jupiter seen by Voyager.

In the infrared (Fig. 16), our phase curve fits moderately well, but does not properly reproduce the slope of the $\alpha = 60°$–$120°$ VIMS observations. We are puzzled by this inconsistency. However, we note that the VIMS phase curve when scaled is fit quite well by the dust component *alone*, as shown. This could indicate that the IR reflectivity of the parent bodies at $\lambda = 2.2$ μm is overestimated in our model. In fact, many asteroids show a strong, wide absorption band near 2 μm (e.g., Vesta, McCord et al., 1970) which could directly explain our fit. Brown et al. (2003) fit the VIMS phase curve alone using power-law distributions of spheres and cubes; our small-particle model improves on their fit, because of both our non-spherical grains and our two-component power-law distribution.

The Voyager observations in forward-scatter are fit in Fig. 17. Calibration uncertainties and intrinsic differences in the brightnesses of the two ring arms affect the absolute values of these observations. However, the slopes of the phase

functions are well-fit by our model. Our fits are comparable to those of Showalter et al. (1987) and Brooks et al. (2003), as neither particle shape nor large bodies affect the high-α phase function.

4.3.2. Fits to spectrum

We have fit the spectrum at backscatter, side-scatter and forward-scatter. The side-scatter spectrum (Fig. 6) is straightforward to interpret, because the observations were all taken with ISS and reflect the same effective phase angle. In our best-fit solution, the ring's red color comes from both the intrinsic color of the large bodies, and red light preferentially scattered by the dust. This finding is consistent with and perhaps suggested by the ISS spectral observations (Fig. 5), which shows the ring to be red at every phase angle from $\alpha = 0°$–$120°$, even though the relative contributions to the light change by a factor of 10 over this phase range (Fig. 4). Because a majority of the light comes from large particles, these must be intrinsically very red. Hektor is among the redder of asteroids; bodies with a flatter spectrum would not be good candidates for ring material source bodies, unless processing within the ring environment reddened their surfaces. Interestingly, we find that although the phase curve of small grains is affected by particle shape, the side-scatter spectrum is not, consistent with the findings of Kolokolova and Lara (2002).

The forward-scatter spectrum (Fig. 18) consists of two of the four NIMS spectra, taken at $\alpha = 177.7°$ and $\alpha = 178.4°$. (The other two spectra lie between these angles and can be easily fit, and are omitted for simplicity.) The fits are excellent. The spectral peak near 2 μm directly correlates with the 15 μm position of r_b, where most particle cross-section resides. (The expected diffraction peak width from such particles can be estimated at $\theta = \lambda/(2\pi r) = 1.2°$, in line with the observations.) In forward-scatter there is essentially no contribution from large particles, so their spectrum does not affect the fit. Because the NIMS data set is of such high quality, it is a strong constraint on $n(r)$, causing our final fits to be very similar to those of Brooks et al. (2003). Fitting the four spectra individually, they found $r_b = 15.5$–22 μm; our model improves on theirs by fitting the spectra with one consistent size distribution. Because light at forward-scatter is predominantly diffraction, the fits are essentially independent of particle shape.

In backscatter (Fig. 19, $\alpha < 12°$), the ring appears red. Fitting this spectrum was challenging, perhaps in part due to the large number of observations taken under different conditions. Our best fits indicate that roughly 2/3 of the ring's flux here comes from large particles. In order to reproduce the spectrum, the bodies must be very red. Our model overestimates the ring's brightness for the two points at 0.7–0.9 μm. We note that the Asteroid Vesta shows a broad absorption band at this location (McCord et al., 1970) which could account for this discrepancy, as our spectral prototype Hektor does not have this feature. It is possible that this is due simply to a poor solution or a problem with

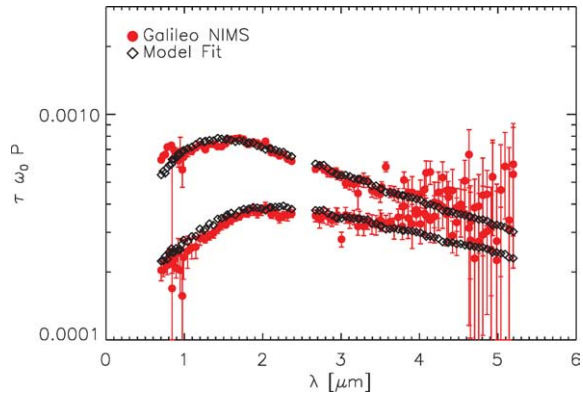

Fig. 18. Forward-scatter spectrum, observed by Galileo's NIMS. The two curves are for ring intercept distances of $1.24R_J$ (top, $\alpha = 178.4°$) and $1.72R_J$ (bottom, $\alpha = 177.7°$).

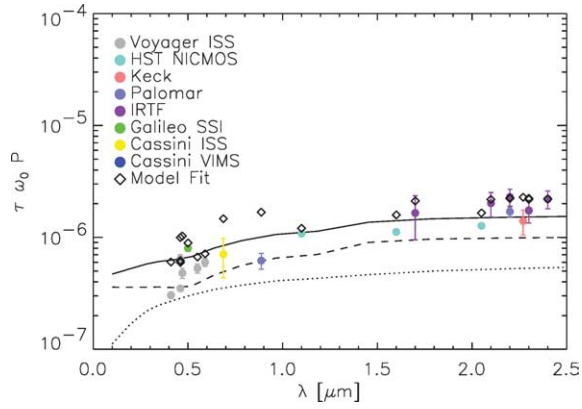

Fig. 19. Backscatter spectrum. Symbols are the same as in Fig. 4. All of the ground-based points are on this plot, which shows significant scatter due in part to the range in phase angle ($\alpha = 0°$–$11°$) and in part to the disparate ways in which each data set was processed. The absolute magnitude of several data sets was scaled as described in the text. Our spectrum does not cross every data point, but does broadly reproduce the slope of the ring's red hue from 0.5–2.5 μm.

the absolute scaling of the data; however, it is true that our fits to these data points would improve if our large bodies showed this feature. In summary, we have not found a large body spectrum that fits the data precisely; however, we predict that the bodies are extremely red, with a slope $d(\text{Albedo})/d\lambda \sim 2\ \mu\text{m}^{-1}$ shortward of 1 μm, and ~ 1 longward of 1 μm. The data suggest a possible band near 0.8 μm.

5. Conclusions

Our major results fall into two categories. First, Cassini ISS observations have filled in many unobserved regions of phase-wavelength space of the jovian ring system. The images have provided new information on the ring's asymmetry and radial profile, and have constrained its side-scattered thickness. We do not detect any asymmetry or longitudinal features in the ring, with the exception of a nebulous trio of interest that may suggest clumps moving through the ring.

Second, our analysis is the first attempt to combine nearly all the Earth- and space-based observations of the main ring's photometry into one coherent picture of the ring's composition. We find that the ring's microscopic dust grains contribute a minority of the ring's reflectivity in backscatter and side-scatter. These dust grains are apparently concentrated near $r = 15$ μm by a process that is not currently understood. Our photometric model indicates that the dust grains are almost certainly not homogeneous spheres; we fit the data well using an ensemble of non-spherical dust grains, superimposed on a population of larger particles. These larger bodies are very red, with their albedo increasing more than linearly with wavelength from $\lambda = 0.4$ μm to $\lambda = 2.5$ μm. We also see suggestive evidence for absorption features on these bodies near 0.8 and 2.2 μm.

Acknowledgments

The Jupiter encounter would have been much less scientifically fruitful were it not for the great efforts of many people. We thank in particular the many engineers involved with making these observations a success; without their hard work, scientific data acquisition at Jupiter would not have been possible. We thank S. Brooks for use of unpublished results; we also thank Brooks, R. Brown, and M. Mishchenko for helpful discussions. J. Spitale's excellent assistance in navigating the images is greatly appreciated. HBT and CCP acknowledge support of the Cassini Project and NASA PGG grant #NAG5-11641. JAB was supported by NASA grant NAGS-11480 and JPL contract #961172; MRS was supported by NASA's Planetary Geology and Geophysics program through RTOP 344-30-21-04.

Appendix A. Non-spherical particles

It is relatively straightforward to compute the phase curve for an ensemble of spherical particles, using the *Mie* scattering method. Standard numerical codes exist (e.g., Bohren and Huffman, 1983) which take as input values a size parameter $x \equiv 2\pi r/\lambda$ and a complex refractive index m and return output values for the phase function $P(\alpha)$ and cross-section Q_{sca}. Given a size distribution $n(r)$ of particles, the total ensemble phase function can be computed by summing over the individual phase functions, as in Eq. (6). On typical workstations, the scattering matrix for a particle of $x = 1000$ can be computed in several seconds. The solution time scales linearly with x, and the upper limit for x is essentially arbitrary, limited only by how well a large particle approximates a smooth, homogeneous sphere.

Although non-spherical particles are often a better reflection of reality than spheres, the computation of scattering coefficients for such particles is significantly more involved. We use the so-called 'T-matrix' method (Waterman, 1971), which numerically computes the propagation of an electromagnetic wave through a medium. The particular implementation of the T-matrix method we employ (Mishchenko and Travis, 1998) models a randomly oriented mixture of monodisperse oblate spheroids. The particles are characterized by an axial ratio $\epsilon = a/b$ in addition to the usual quantities of x and refractive index m. The present code computes the scattering matrix for particles up to roughly $x = 160$ (for $\epsilon = 1.5$); such a computation may take ten hours of CPU time. The computation time scales as x^3; the upper size limit is determined largely by the internal accuracy to which computations can be performed. Typically, the non-spherical phase functions are characterized by a reduced backscatter 'glory' near $\alpha = 0°$, and increased scattering at mid-phase ($\alpha = 30°$–$90°$). Forward of $\alpha = 90°$, the effect of particle shape is much less pronounced, as P is dominated by diffraction.

The upper limit of $x = 160$ is frustratingly close to the largest particles which we need consider: Work by Brooks et al. (2003) and our own earlier *Mie* fits suggested that a majority of the particle surface area is in grains of 10–20 μm radius. For $\lambda = 0.5$ μm, $r = 20$ μm corresponds to $x = 250$. Therefore, the method of Mishchenko and Travis (1998) is almost but not quite usable.

We have observed, however, that the behavior of the T-matrix phase function P_T for large values of x can in a very simple way be extrapolated from lower values. Mishchenko et al. (1997) presents figures (their Plate 2) which plot the ratio of *Mie* and T-matrix phase functions as a function of x. By examining these figures, a broad trend can be observed, in that the ratio P_T/P_{Mie} at a given α follows a generally smooth, predictable trend. We have extrapolated this ratio, along with the known values of $P_{Mie}(x,\alpha)$, in order to predict values of $P_T(x,\alpha)$ for a limited range of x, typically up to $x \sim 300$.

In all cases, we average together values of P_T for an ensemble of particle shapes, usually with $\epsilon = 1.0$, 1.2, 1.4, 1.6, 1.8, and 2.0. The maximum value of x for which P_T can be directly computed increases with decreasing ϵ. The larger particles in our model are therefore weighted toward lower values of ϵ.

It would be preferable, of course, to calculate values of P_T directly using formally robust methods; however, given that this is not possible with current computational techniques, we believe that our method provides a significant advantage over using *Mie* scattering to approximate the scattering from non-spherical particles. We note that semi-empirical approaches to light-scattering have a long history in the literature; for instance, the model of Pollack and Cuzzi (1980) has been extensively used to model planetary rings.

References

Becklin, E.E., Wynn-Williams, C.G., 1979. Detection of Jupiter's ring at 2.2 micron. Nature 279, 400–401.

Bohren, C.F., Huffman, D.R., 1983. Absorption and Scattering of Light by Small Particles. Wiley, New York.

Brooks, S.M., 2003. Jupiter's ring system revealed: a deeper understanding from Galileo visible and infrared observations. PhD thesis. University of Colorado, Boulder.

Brooks, S.M., Esposito, L.W., Showalter, M.R., Throop, H.B., 2003. The size distribution of Jupiter's main ring from Galileo imaging and spectroscopy. Icarus. Submitted for publication.

Brown, R.H., Baines, K.H., Bellicci, G., Bibring, J.-P., Buratti, B.J., Capaccioni, F., Cerroni, P., Clark, R.N., Coradini, A., Cruikshank, D.P., Drossart, P., Formisano, V., Jaumann, R., Langevin, Y., Matson, D.L., McCord, T.B., Mennella, V., Nelson, R.M., Nicholson, P.D., Sicardy, B., Sotin, C., Amici, S., Chamberlain, M.A., Filacchioni, G., Hansen, G., Hibbitts, K., Showalter, M., 2003. Observations with the Visual and Infrared Mapping Spectrometer (VIMS) during Cassini's flyby of Jupiter. Icarus 164, 461–470.

Burns, J.A., Showalter, M.R., Morfill, G.E., 1984. The ethereal rings of Jupiter and Saturn. In: Brahic, A., Greenberg, R. (Eds.), Planetary Rings. Univ. of Arizona Press, Tucson, pp. 200–272.

Burns, J.A., Showalter, M.R., Hamilton, D.P., Nicholson, P.D., de Pater, I., Ockert-Bell, M.E., Thomas, P.C., 1999. The formation of Jupiter's faint rings. Science 284, 1146–1150.

Canup, R.M., Esposito, L.W., 1997. Evolution of the G ring and the population of macroscopic ring particles. Icarus 126, 28–41.

Cruikshank, D.P., Dalle Orre, C.M., Roush, T.L., Geballe, T.R., Owen, T.C., de Bergh, C., Cash, M.D., Hartmann, W.K., 2001. Constraints on the composition of Trojan Asteroid 624 Hektor. Icarus 153, 348–360.

Cuzzi, J.N., French, R.G., Dones, L., 2002. HST multicolor (255–1042 nm) photometry of Saturn's main rings. I: radial profiles, phase and opening angle variations, and regional spectra. Icarus 158, 199–223.

de Pater, I., Showalter, M.R., Burns, J.A., Nicholson, P.D., Liu, M.C., Hamilton, D.P., Graham, J.R., 1999. Keck infrared observations of Jupiter's ring system near Earth's 1997 ring plane crossing. Icarus 138, 214–223.

Dones, L., Cuzzi, J.N., Showalter, M.R., 1993. Voyager photometry of Saturn's A ring. Icarus 105, 184–215.

Ferrari, C., Brahic, A., 1997. Arcs and clumps in the Encke division of Saturn's rings. Planet. Space Sci. 45, 1051–1067.

Helfenstein, P., Currier, N., Clark, B.E., Veverka, J., Bell, M., Sullivan, R., Klemaszewski, J., Greeley, R., Pappalardo, R.T., Head, J.W., Jones, T., Klaasen, K., Magee, K., Geissler, P., Greenberg, R., McEwen, A., Phillips, C., Colvin, T., Davies, M., Denk, T., Neukum, G., Belton, M.J.S., 1998. Galileo observations of Europa's opposition effect. Icarus 135, 41–63.

Horanyi, M., Cravens, T.E., 1996. The structure and dynamics of Jupiter's ring. Nature 381, 293–295.

Jewitt, D.C., Danielson, G.E., 1981. The jovian ring. J. Geophys. Res. 86, 8691–8697.

Kolokolova, L., Lara, L., 2002. Color of an ensemble of particles with a wide power-law size distribution. In: Mishchenko, M.I. (Ed.), Sixth Conference on Light Scattering by Nonspherical Particles.

McCord, T.B., Adams, J., Johnson, T., 1970. Asteroid Vesta: spectral reflectivity and compositional implications. Science 168, 1445–1447.

McGuire, A.F., Hapke, B.W., 1995. An experimental study of light scattering by large, irregular particles. Icarus 113, 134–155.

McMuldroch, S., Pilorz, S.H., Danielson, G.E., the NIMS Science Team, 2000. Galileo NIMS near-infrared observations of Jupiter's ring system. Icarus 146, 1–11.

Meier, R., Smith, B.A., Owen, T.C., Becklin, E.E., Terrile, R.J., 1999. Near infrared photometry of the jovian ring and Adrastea. Icarus 141, 253–262.

Mishchenko, M.I., Macke, A., 1997. Asymmetry parameters of the phase function for isolated and densely packed spherical particles with multiple internal inclusions in the geometric optics limit. J. Quant. Spectrosc. Radiat. Transfer 57, 767–794.

Mishchenko, M.I., Travis, L.D., 1998. Capabilities and limitations of a current Fortran implementation of the T-matrix method for randomly oriented, rotationally symmetric scatterers. J. Quant. Spectrosc. Radiat. Transfer 60, 309–324.

Mishchenko, M.I., Travis, L.D., Kahn, R.A., West, R.A., 1997. Modeling phase functions for dust-like tropospheric aerosols using a shape mixture of randomly oriented polydisperse spheroids. J. Geophys. Res. 102, 13543–13553.

Neugebauer, G., Becklin, E.E., Jewitt, D.C., Terrile, R.J., Danielson, G.E., 1981. Spectra of the jovian ring and Amalthea. Astron. J. 86, 607–610.

Nicholson, P.D., Matthews, K., 1988. Near-infrared observations of the jovian ring and small satellites. Icarus 93, 331–346.

Northrop, T.G., Mendis, D.A., Schaffer, L., 1989. Gyrophase drifts and the orbital evolution of dust at Jupiter's gossamer ring. Icarus 79, 101–115.

Ockert-Bell, M.E., Burns, J.A., Daubar, I.J., Thomas, P.C., Veverka, J., Belton, M.S.J., Klaasen, K.P., 1999. The structure of Jupiter's ring system as revealed by the Galileo imaging experiment. Icarus 138, 188–213.

Orton, G., 57 colleagues, 1995. Collision of Comet Shoemaker–Levy 9 with Jupiter observed by the NASA Infrared Telescope Facility. Science 267, 1277–1282.

Pollack, J.B., Cuzzi, J.N., 1980. Scattering by nonspherical particles of size comparable to a wavelength: a new semi-emprical theory and its application to tropospheric aerosols. J. Atmos. Sci. 37, 868–881.

Porco, C.C., Danielson, G.E., 1982. The periodic variation of spokes in Saturn's rings. Astron. J. 87, 826–833.

Porco, C.C., West, R.A., McEwen, A., DelGenio, A.D., Ingersoll, A.P., Thomas, P., Squyres, S., Dones, L., Murray, C.D., Johnson, T.V., Burns, J.A., Brahic, A., Neukum, G., Veverka, J., Barbara, J.M., Denk, T., Evans, M., Ferrier, J.J., Geissler, P., Helfenstein, P., Roatsch, T., Throop, H., Tiscareno, M., Vasavada, A., 2003. Cassini imaging of Jupiter's atmosphere, satellites, and rings. Science 299, 1541–1547. Supporting online material: http://www.sciencemag.org/cgi/content/full/299/5612/1541/.

Showalter, M.R., 1996. Saturn's D ring in the Voyager images. Icarus 124, 677–689.

Showalter, M.R., 1998. Detection of centimeter-sized meteoroid impact events in Saturn's F ring. Science 282, 1099–1102.

Showalter, M.R., Cuzzi, J.N., 1993. Seeing ghosts: photometry of Saturn's G ring. Icarus 103, 124–143.

Showalter, M.R., Burns, J.A., Cuzzi, J.N., Pollack, J.B., 1987. Jupiter's ring system: new results on structure and particle properties. Icarus 69, 458–498.

Showalter, M.R., Pollack, J.B., Ockert, M.E., Doyle, L.R., Dalton, J.B., 1992. A photometric study of Saturn's F ring. Icarus 100, 394–411.

Showalter, M.R., Hamilton, D.P., Burns, J.A., de Pater, I., Simonelli, D.P., 2001. Structure of Jupiter's main ring and halo from Galileo SSI and Earth-based images. In: Bagenal, F. (Ed.), Jupiter: Planet, Satellites, and Magnetosphere, pp. 101–102.

Showalter, M.R., Burns, J.A., de Pater, I., Hamilton, D.P., Horanyi, M., 2003. Recent Hubble observations of Jupiter's ring system. Bull. Am. Astron. Soc. 35, 930.

Smith, B.A., Reitsema, H.J., 1980. CCD observations of Jupiter's ring and Amalthea. In: Satellites of Jupiter. IAU Colloq. Series, vol. 57.

Squyres, S.W., Veverka, J., 1981. Voyager photometry of surface features on Ganymede and Callisto. Icarus 46, 137–155.

Thomas, P.C., Burns, J.A., Rossier, L., Simonelli, D., Veverka, J., Chapman, C.R., Klaasen, K., Johnson, T.V., Belton, M.J., 1998. The small inner satellites of Jupiter. Icarus 135, 360–371.

Throop, H.B., Esposito, L.W., 1998. G ring particle sizes derived from ring plane crossing observations. Icarus 131, 152–166.

Waterman, P.C., 1971. Symmetry, unitarity, and geometry in electromagnetic scattering. Phys. Rev. D 3, 825–839.